Journal of Energy Storage 153 (2026) 121058

Contents lists available at ScienceDirect

Journal of Energy Storage

journal homepage: www.elsevier.com/locate/est

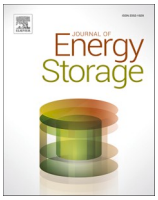

Research papers

# Multiscale pore engineering in separators for aqueous Zn-ion batteries in infrastructure applications

Guanghui Tao [a], Yurong You [a,*], Zhaolong Liu [a], Shuyang Bian [a], Ruidan Liu [a], Long Yuan [a], Jian Chen [a], Linfeng Hu [a], Pan Feng [a,*]

[a] State Key Laboratory of Engineering Materials for Major Infrastructure, School of Materials Science and Engineering, Southeast University, Nanjing, 211189, China

ARTICLE INFO

*Keywords:*
Cement paste separators
Etching
Pore structures
Energy storage

ABSTRACT

Infrastructure materials offer immense potential as carriers for large-scale structural energy storage systems (SESSs). Among them, cement-based separators are particularly attractive for their dual functionality—facilitating ion transport while bearing structural loads. However, rationally engineering their micropore architecture to optimize electrochemical properties remains a critical challenge. Here, we report a simple, low-cost and controllable etching strategy to fabricate porous cement paste separators (CPSs) by selectively removing hydration products. The resulting microstructure exhibits markedly increased porosity, particularly within the 0.005–1.0 μm range. A predictive model linking porosity to conductivity identifies 0.05–0.85 μm pores as the dominant contributor to ionic transport. The optimized CPSs with a 25% mass loss achieve a synergistic balance between enhanced ion conduction (12.25 mS $cm^{-1}$) and mechanical robustness (18.93 MPa). Zn||Zn symmetrical cells incorporating this CPSs exhibit highly stable cycling with minimal voltage fluctuation, indicative of homogeneous zinc deposition and stripping, as further supported by finite element simulations. When integrated into SESSs, the optimized CPSs deliver excellent rate performance and cycling stability. This work provides a scalable route to design multifunctional cement-based components, advancing the development of energy-storing infrastructure materials.

## 1. Introduction

With the accelerating depletion of non-renewable energy resources and growing environmental concerns, the global demand for renewable and clean energy sources—such as solar and wind power—has become increasingly urgent [1–3]. However, the inherent intermittent and volatile nature of these sources create significant challenges, underscoring the critical need for efficient, safe, and cost-effective energy storage systems to balance energy supply and demand [4–6]. Among current storage technologies, Li-ion batteries (LIBs) have achieved remarkable commercial success and are widely used in daily applications [7]. Nevertheless, the limited availability and high reactivity of lithium introduce key challenges, including elevated production costs and safety risks, which constrain the scalability of LIB deployment [7,8]. These limitations highlight the urgent need for alternative energy storage systems that combine low cost, inherent safety, and suitability for large-scale implementation.

Aqueous zinc-ion batteries (AZIBs) are considered promising candidates for large-scale energy storage systems due to their inherent safety, low cost, environmental friendliness, high theoretical capacity of the zinc metal anode (820 mAh $g^{-1}$), and suitable redox potential (−0.76 V vs. SHE) [9]. When integrated into civil infrastructures—such as in non-critical or non-load-bearing components of buildings, roads, and bridges—AZIBs could enable a transformative strategy. This approach envisions converting vast built environments into large-scale structural energy storage systems (SESSs) (as shown in Fig. 1 (a, b)) where specialized battery components primarily provide electrochemical functionality rather than structural support. The key component of SESSs is separator, which serves not only as a physical barrier between the positive and negative electrodes but also plays a critical role in regulating ion transport kinetics and influencing the interfacial electrochemical environment. Although widely used, conventional separators—such as glass fiber separators and cellulose-based separators—often exhibit loose porous structures and poor mechanical strength [10]. These limitations make them ineffective in suppressing zinc dendrite penetration and are inadequate to meet the demanding

* Corresponding authors.
*E-mail addresses:* youyr@seu.edu.cn (Y. You), pan.feng@seu.edu.cn (P. Feng).

https://doi.org/10.1016/j.est.2026.121058
Received 11 November 2025; Received in revised form 18 January 2026; Accepted 7 February 2026
Available online 11 February 2026

load-bearing requirements of SESSs [11]. In this context, cement-based materials emerge as particularly promising candidates. Their inherent properties—such as abundant resources, exceptional durability, robust mechanical property, and advantages in cost and availability—are well-suited to address these challenges [12]. Importantly, their intrinsic pore network makes them well-suitable as separators by providing space for electrolyte retention and ion transport, while offering tunable pore morphologies to optimize performance [13,14]. Coupled with their excellent electrical insulation and high mechanical strength, cement-based materials could serve as a functional layer in future SESSs, contributing to the vision of embedding energy storage capabilities into built environments like buildings and bridges.

The energy density of SESSs is largely governed by the ionic conductivity of the cement-based separators. Recent approaches have incorporated conductive polymers such as polyacrylic acid (PAA), polyvinyl alcohol (PVA), and polyacrylamide (PAM) into cementitious matrices to enhance ionic conductivity [15–18]. Nevertheless, these polymers often agglomerate during mixing, which disrupts cement hydration and compromises mechanical performance. Moreover, their flammability and toxicity introduce safety risks to the overall system [19,20]. To address these limitations, tailoring the intrinsic pore structures of cement-based separators has emerged as a promising route to enhance electrochemical performance. Increasing water-cement ratio can marginally raise porosity and improve specific capacitance, but the extent of enhancement is limited [21]. Gas-foaming technique is a more effective strategy by introducing air to substantially increase porosity and, consequently, electrochemical performance [22–27]. However, the random distribution and uncontrolled size of these bubbles often lead to non-uniform ion pathways and localized current density spikes, which can trigger dendrite formation on electrodes [28]. Additionally, the introduction of excessive and large bubbles significantly compromises compressive strength, highlighting the inherent trade-off between pore structure optimization and mechanical integrity [29,30]. Pore connectivity also plays a crucial role in facilitating ion transport [24]. Methods such as fiber reinforcement (e.g., hemp fibers) have been employed to improve pore connectivity and benefit the electrochemical properties. However, these modifications often severely weaken mechanical strength [31]. Therefore, to advance the practical implementation of high-performance SESSs, it is imperative to develop a controllable fabrication strategy for cement-based separators with engineered pore structures that simultaneously enable rapid ion transport and maintain robust mechanical performance.

A conventional surface treatment technique—chemical etching—is innovatively employed to selectively dissolve the hydration products in cement paste separators (CPSs), enabling precise tailoring of their pore structures [32]. The chemical etching method for fabricating porous CPSs offers a compelling combination of advantages rooted in material sustainability, process simplicity, and functional innovation. It utilizes abundantly available and low-cost cementitious materials as the raw source, enabling scalable and economical production. The process selectively dissolves inherent components to create an interconnected porous network without requiring additional templates, thereby simplifying fabrication and avoiding impurity introduction. Furthermore, the pore structures are highly tunable by adjusting etching parameters and the initial composition, allowing for tailored design to meet specific electrochemical performance requirements. This synergy of cost-effectiveness, streamlined processing, functional conversion, and structural designability positions etching-derived porous cement separators as a promising platform for next-generation energy storage devices. More importantly, the etching method stands in contrast to cement-based separators fabricated via the gas-foaming technique, which typically feature irregularly distributed macropores, as presented

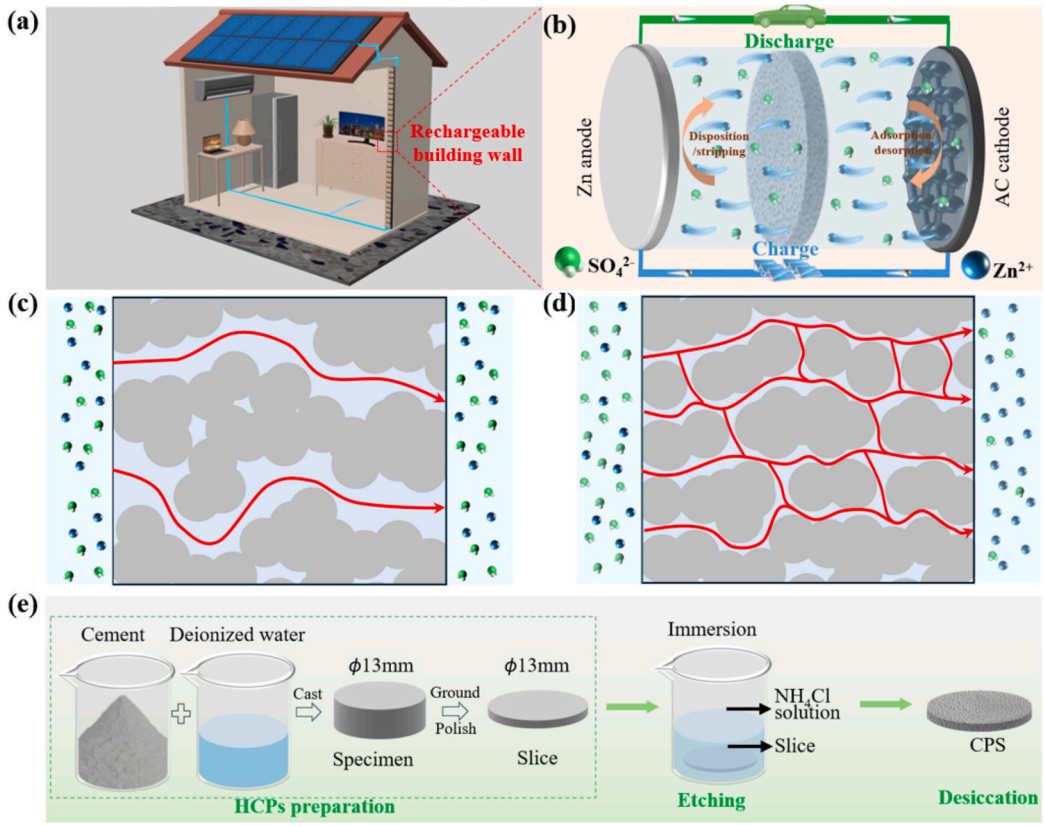


**Fig. 1.** Schematic illustration of the design concept and fabrication strategy of CPSs for structural energy storage systems. (a) Conceptual diagram of SESSs. (b) Configuration of the ZIHC employing CPSs, Zn anode and active carbon (AC) cathode. (c) The fabrication process for CPSs. (d) The CPSs with irregularly distributed macropores prepared by gas-foaming. (e) The CPSs with uniformly distributed multiscale pores obtained through the controllable etching method.

in Fig. 1 (c). While these macropores support rapid and substantial ion transport, they result in an inhomogeneous flux of zinc ions across the electrode surface and exhibit limited selective screening ability. In contrast, separators produced by the etching method possess a uniform and densely packed array of multiscale pores, as shown in Fig. 1 (d). These multiscale pores not only enable efficient and fast zinc-ion transport but also promote a homogeneous ion flux along the electrode surface, thereby improving the stability of electrode reactions and enhancing overall battery performance.

In this study, microporous cement paste separators (CPSs) were produced by the etching method to engineer their porous structure, as shown in Fig. 1 (e). To better assess the effect of optimized pore structures on the electrochemical performance, CPSs were integrated into aqueous Zn-ion hybrid supercapacitors (ZIHCs), selected for their intrinsic safety, low cost of Zinc, and prior successful demonstrations of CPS-ZIHC systems with excellent specific energy density, high areal energy density, and robust cycling stability, as illustrated in Fig. 1 (b) [26,27]. A series of CPSs with varying mass losses were systematically characterized to investigate microstructural changes induced by chemical etching. Essential properties including ionic conductivity, electrolyte uptake, and compressive strength were systematically quantified. Furthermore, the electrochemical behavior of Zn||Zn symmetric cells and ZIHCs incorporating differentially etched CPSs was thoroughly evaluated. Finally, finite element simulations were employed to investigate the effects of pore structures on the governing electric field and zinc concentration distribution. This work enables the scalable design of multifunctional cement-based components, driving progress toward energy-efficient infrastructure.

## 2. Materials and methods

### 2.1. Materials

Reference cement (P·I 42.5) was supplied by Qufu Zhonglian cement co., ltd. zinc metal foil (50 μm) and commercial active carbon (AC, XFP01, 1800 $m^2\ g^{-1}$) was sourced from Shanghai Weidi metal material co., ltd. and XFNANO corporation, respectively. Polyvinylidene difluoride (PVDF) was purchased from AKEMA, acetylene black from 3 a, ammonium chloride ($NH_4Cl$) from Meryer (Shanghai) biochemical technology co. ltd., and *N*-methylpyrrolidone (NMP) from Macklin. Aluminum oxide (α-$Al_2O_3$) and zinc sulfate heptahydrate ($ZnSO_4{\cdot}7H_2O$) were provided by Aladdin

### 2.2. Preparation of CPSs

The preparation of CPSs involved three steps (Fig. 1 (e)): (i) Hardened cement pastes (HCPs) preparation: cement pastes were prepared with a *w/c* ratio of 0.5, cast in rubber molds with a diameter of 13 mm and a thickness of 5 mm, demolded after 24 h, and cured at room temperature (20 ± 2 °C) for 28 days. After curing, the specimens were ground and polished into slices with a thickness of 1 mm. (ii) Etching: the slices were immersed in deionized water, placed under a vacuum (−0.1 MPa) for 6 h, and then transferred into a 5 mol $L^{-1}$ $NH_4Cl$ solution to dissolve the hydration products. Mass loss was monitored every 10 min to control porosity. (iii) Desiccation: the etched slices were rinsed in deionized water (3 h) to remove residual $NH_4Cl$ and then dried at 40 °C for 3 days to constant weight, yielding porous CPSs. Samples with mass loss of *x*% were labeled as ML*x*.

### 2.3. Assembly of ZIHCs

AC cathodes were prepared by mixing active carbon, acetylene black and PVDF in a mass ratio of 8:1:1. The powder was mixed with NMP according to a solid-liquid mass ratio of 20:1,followed by blade-coating onto stainless steel mesh, achieving an average mass loading of ~2.48 mg $cm^{-2}$ as detailed in literature [26,27], as shown in Fig. S1 (a). Zinc foil with a thickness of 50 μm was used as the Zn anode. Circular electrodes with a diameter of 12 mm were assembled by connecting the AC cathode and Zn anode with conductive tabs. Prior to assembly, the CPSs were soaked into 2 M $ZnSO_4$ electrolyte under vacuum (−0.1 MPa) for 7 days (a period sufficient for ionic conductivity stabilization based on prior studies [26]) to ensure complete electrolyte wetting of the pore network. Based on the deliberately large immersion solution volume to separator mass ratio, which provided significant buffering capacity, the overall pH of the solution remained stable (approximately 3.8) with no significant changes observed during the immersion period. ZIHCs were assembled in a sandwich configuration (anode-separator-cathode) using CPSs as separators as illustrated in Fig. S1 (b), with 2 M $ZnSO_4$ as electrolyte. To avoid the problems of evaporation and leakage, these were designed within a hermetically aluminum pouch cell. Similarly, Zn||Zn symmetrical cells were assembled using CPSs and two Zn anodes to evaluate the stability of the Zn electrode.

### 2.4. Testing and simulation

#### 2.4.1. X-ray diffraction (XRD)

The phase composition of CPSs was analyzed by XRD (Bruker D8-discover) with Cu Kα radiation. XRD patterns were observed under a 2θ range of 10–40°, and the samples were scanned at a step width of 0.02° with a scanning rate of 0.15 s per step. To quantitatively analyze the phase composition, all samples were ground into powder and mixed with a mass fraction of 15–20% α-$Al_2O_3$ as the internal reference. Quantitative XRD (QXRD) analysis was performed using Topas software. To better compare compositional variations across samples with different mass losses, the mass fractions of each phase were converted into mass per unit volume (i.e., g $cm^{-3}$) by multiplying their respective densities.

#### 2.4.2. Scanning electron microscopy (SEM)

The cross-sectional microstructure morphology of CPSs was examined using a field-emission scanning electron microscope (FE-SEM, Nova Nano SEM450) operated in secondary electron (SE) mode. To enhance conductivity and surface resolution, a thin platinum coating was applied prior to imaging.

The etching depth was quantitatively determined by analyzing the cross-sectional distribution of pore pixels using backscattered electron (BSE) imaging coupled with elemental mapping. Similarly, the penetration depth of $ZnSO_4$ electrolyte was evaluated by mapping the spatial distribution of zinc (Zn) under identical analytical conditions.

Sample preparation followed a systematic protocol. Air-dried CPSs were longitudinally sectioned along the etching direction to expose internal cross-section. The sections were then embedded in low-viscosity epoxy resin under vacuum to preserve the pore structure. After curing at ambient temperature (25 ± 2 °C), the embedded samples were subjected to sequential metallographic preparation. This involved coarse grinding with silicon carbide abrasive papers (1000 and 2000 grit), followed by multi-stage precision polishing using diamond pastes of 9 μm, 3 μm and 1 μm particle sizes for durations of 15 min, 60 min, and 120 min respectively. Between each stage, specimens were ultrasonic cleaned in anhydrous isopropyl alcohol to remove surface residues and maintain interfacial clarity.

#### 2.4.3. Thermogravimetric analysis (TGA)

TGA was conducted using a Netzsch STA 449 F3 instrument to investigate the phase composition of CPSs. Samples underwent dynamic heating in a nitrogen atmosphere to prevent oxidative decomposition, with the temperature being increased steadily at 10 °C $min^{-1}$ from 30 °C up to 1000 °C.

#### 2.4.4. Mercury intrusion porosimetry (MIP)

Pore structure parameters of CPSs were characterized via MIP (AutoPore Iv 9510). Assuming a cylindrical pore geometry, the pore

diameter $d$ is calculated from the applied pressure $P$ using the Washburn eq. [33],

$$d = -\frac{4\gamma\cos\theta}{P} \tag{1}$$

where $\gamma$ is the surface tension of mercury and $\theta$ is the contact angle between mercury and the pore wall.

Key pore characteristics—including porosity, specific surface area, pore size distribution (PSD), critical diameter, median diameter and average diameter—were obtained from the MIP data. Porosity was derived from the maximum cumulative intrusion volume, while the critical diameter was identified as the inflection point of the cumulative pore volume curve or the peak in the corresponding logarithmic differential curve [33].

In addition, pore connectivity $\eta$ and tortuosity $\tau$ were estimated using the ink-bottle porosity method [34,35],

$$\eta = \frac{\varphi - \varphi_{\text{ink}}}{\varphi} \times 100\% \tag{2}$$

$$\tau = 4.6242\ln\left(\frac{4.996}{1-\alpha_{en}} - 1\right) - 5.8032 \tag{3}$$

where $\varphi$ is the total porosity, $\alpha_{\text{en}}$ is the ratio of $\varphi_{\text{ink}}$ to $\varphi$. $\varphi_{\text{ink}}$ is defined as the ratio of retained mercury volume to total intruded mercury after pressure release [36].

### 2.4.5. Electrolyte uptake

The electrolyte uptake (EU) of CPSs was measured by immersing air-dried samples in a $ZnSO_4$ electrolyte solution for 7 d within a vacuum desiccator to ensure full infiltration. After immersion, excess surface electrolyte was gently removed using filter paper. The EU was then calculated as follows [37]:

$$\text{EU} = \frac{w_a - w_b}{w_b} \times 100\% \tag{4}$$

where $w_{\text{b}}$ and $w_{\text{a}}$ are the masses of CPSs before and after electrolyte adsorption, respectively.

### 2.4.6. Compressive strength

The CPSs were machined into cubic specimens with dimensions of 1 × 1 × 1 mm. It should be noted that such a very small specimen size may lead to a size effect and likely overestimate the apparent mechanical strength. This choice was necessitated by the millimeter-scale thickness of the CPSs, as well as the need to ensure a consistent evaluation of the etching gradient while avoiding the influence of microstructural non-uniformity. Compressive strength was measured using a symmetric tension-compression testing system (IBTC-2000) at a loading rate of 1 N $s^{-1}$. The compressive strength (σ, MPa) was calculated using the following equation:

$$\sigma = \frac{P}{A} \tag{5}$$

where $P$ and $A$ represent the peak load (N) and compressive area ($mm^2$), respectively. The compressive strength of CPSs was evaluated in two conditions: first in the as-fabricated state, and then after immersion in a 2 M zinc sulfate aqueous solution for 7 days to assess its stability under simulated operating conditions. For each group, a minimum of five samples were tested.

### 2.4.7. Electrochemical measurements

Electrochemical impedance spectroscopy (EIS) and Cyclic voltammetry (CV) were carried out using an electrochemical workstation (CS Studio6). EIS measurements were performed over the frequency range of 0.1–$10^6$ Hz with a perturbation amplitude of 5 mV amplitude at open-circuit voltage. Each test was repeated three times to evaluate electrochemical stability and reversibility. Galvanostatic charge-discharge (GCD) measurements were conducted using a battery cycler (CT3001A, LANHE) to assess the rate capability and cycling performance of ZIHCs. All electrochemical tests were carried out within a voltage window of 0.2–1.8 V at a controlled ambient temperature of 20 ± 2 °C.

For ionic conductivity measurements, two stainless steel plates with a thickness of 0.1 mm were placed on opposite sides of the CPSs. The ionic conductivity ($IC$, mS $cm^{-1}$) was calculated at room temperature(20 ± 2 °C) from the EIS Nyquist plot using the following equation:

$$IC = \frac{1000d}{R_s \times A} \tag{6}$$

where $d$ is the thickness of the CPSs (cm), $R_s$ is the solution resistance (Ω) determined from the intercept of the EIS curve with the real axis, and $A$ is the contact area between stainless steel and CPSs (1.13 $cm^2$).

The electrochemical parameters including specific capacity $C_s$ (mAh $g^{-1}$), areal capacity $C_a$ (mAh $cm^{-2}$), energy density $E_s$ (Wh $kg^{-1}$), areal energy density $E_a$ (Wh $m^{-2}$), power density $P_s$ (W $kg^{-1}$), areal powder density $P_a$ (Wh $m^{-2}$) of the ZIHCs were derived from the GCD curves and were calculated using the following equations:

$$C_s = \frac{1000 \times I \times t}{m} \tag{7}$$

$$C_a = \frac{1000 \times I \times t}{A} \tag{8}$$

$$E_s = \frac{1000 \times \int IV(t)dt}{m} \tag{9}$$

$$E_a = \frac{10000 \times \int IV(t)dt}{A} \tag{10}$$

$$P_s = \frac{E_s}{t} \tag{11}$$

$$P_a = \frac{E_a}{t} \tag{12}$$

where $I$ represents the discharge current (A), $t$ represents the discharge time (h), and $m$ represents the mass of active carbon of cathode (g), $V(t)$ represents the instantaneous discharge voltage (V), and $A$ represents the area (1.13 $cm^2$) of cathode. Unless otherwise specified, the specific capacity, energy density, and power density reported in this work are calculated based on the mass of the activated carbon in the cathode.

### 2.4.8. Finite element simulations

Finite element simulations were conducted to elucidate the effects of pore size, porosity and pore connectivity within CPSs on the local electric field and $Zn^{2+}$ ion distribution. The "Tertiary Current Distribution, Nernst-Planck" model was employed to solve the electric field distribution and ion concentration fields. The ion transport process was described by Fick's first law of diffusion coupled with the Nernst-Planck equation. The simulation domain consisted of two electrodes (10 μm in length) separated by a 10 μm electrolyte region incorporating the CPSs structure. The positive electrode was defined as a zero-potential boundary, while the negative electrode was assigned a polarization voltage corresponding to the applied overpotential. The initial $Zn^{2+}$ concentration was set to 2 M, and the diffusion coefficient of $Zn^{2+}$ in the electrolyte was defined as $1 \times 10^{-14}$ $m^2$ $s^{-1}$. The exchange current density was set to 1 mA $cm^{-2}$, and the system temperature was maintained at 298 K. For simplicity, the interfacial reaction kinetics at the Zn electrode were assumed to be spatially uniform.

## 3. Results

### 3.1. Phase and microstructure evolution of CSPs

Fig. 2 (a) displays the X-ray Diffraction (XRD) patterns of CPSs, revealing a complex mixture of unhydrated cement clinkers ($C_3A$, $C_3S$, $C_2S$, and $C_4AF$) and hydration products (C-S-H, CH, $CaCO_3$, and AFt phase). Fig. 2 (c) quantitatively illustrates the evolution of volume-based phase composition in response to progressive mass loss. Samples exhibiting a mass loss of *x*% are denoted as ML*x*, corresponding to ML0 ~ ML30 for losses of 0% ~ 30% respectively. Notably, the CH content exhibits a monotonic decline across the ML0-ML10 series and approaches depletion in the groups of ML15-ML30, indicating effective removal of CH through extended etching [38]. The amorphous phase content also decreases with increasing mass loss, likely due to calcium leaching from the C-S-H gel [39,40]. In parallel, the quantities of crystalline clinker phases ($C_3A$, $C_3S$, and $C_2S$) decline as well, which may be attributed to the consumption of CH. The reduction in CH may enhance contact between residual unhydrated clinkers and pore solutions, thus promoting secondary hydration.

Fig. 2 (b) presents the XRD patterns of CPSs after immersion in $ZnSO_4$ electrolyte. Two additional crystalline phases—zinc sulfate hydroxide hydrate ($Zn_4(OH)_6SO_4{\cdot}4H_2O$, ZSH) and gypsum—are observed, supplementing those detected in the unsoaked samples (Fig. 2 (a)). Quantitative phase analysis in Fig. 2 (d) reveals distinct trends for these newly formed phases with increasing mass loss. Gypsum content increases steadily with mass loss up to 20%, beyond which it begins to decline. A similar trend is observed for ZSH, which reaches a maximum at 25% mass loss and then drops significantly at 30% mass loss. These decreases at higher mass loss levels may result from the depletion of CH that can continually supply calcium ions for their formation.

Fig. 2 (e) and (f) illustrate TG/DTG curves of CPSs before and after immersion in $ZnSO_4$ electrolyte. Complementary volume-based composition data are provided in Fig. S4. At 20% mass loss, CH becomes nearly undetectable. The presence of gypsum in $ZnSO_4$-treated samples corroborates the XRD findings. Furthermore, the ML15–30&$ZnSO_4$ groups retain over 85% of their original mass when temperature up to 700 °C, indicating excellent thermal stability. This property is particularly advantageous for separator materials, as it implies a lower risk of structural degradation or thermal decomposition of separator during device operation. Such robustness is expected to contribute to improved long-term cycling stability and enhanced safety in energy storage devices. To assess the impact of the drying process at 40 °C on the structure, the linear dimensions of the CPSs were measured before and after drying. The results show that under the mild condition of 40 °C, the linear shrinkage of the samples was confined to 1%–2%, demonstrating good macroscopic dimensional stability.

Fig. 2 (g-i) exhibits the microstructure evolution of CPSs before and after etching and subsequent $ZnSO_4$ immersion. The unetched HCP (Fig. 2 (g)) displays a dense matrix dominated by C-S-H gel, with embedded AFt crystals, CH, and pores ranging from the nanometer scale to a few microns. In contrast, the etched CPSs (Fig. 2 (h)) exhibits

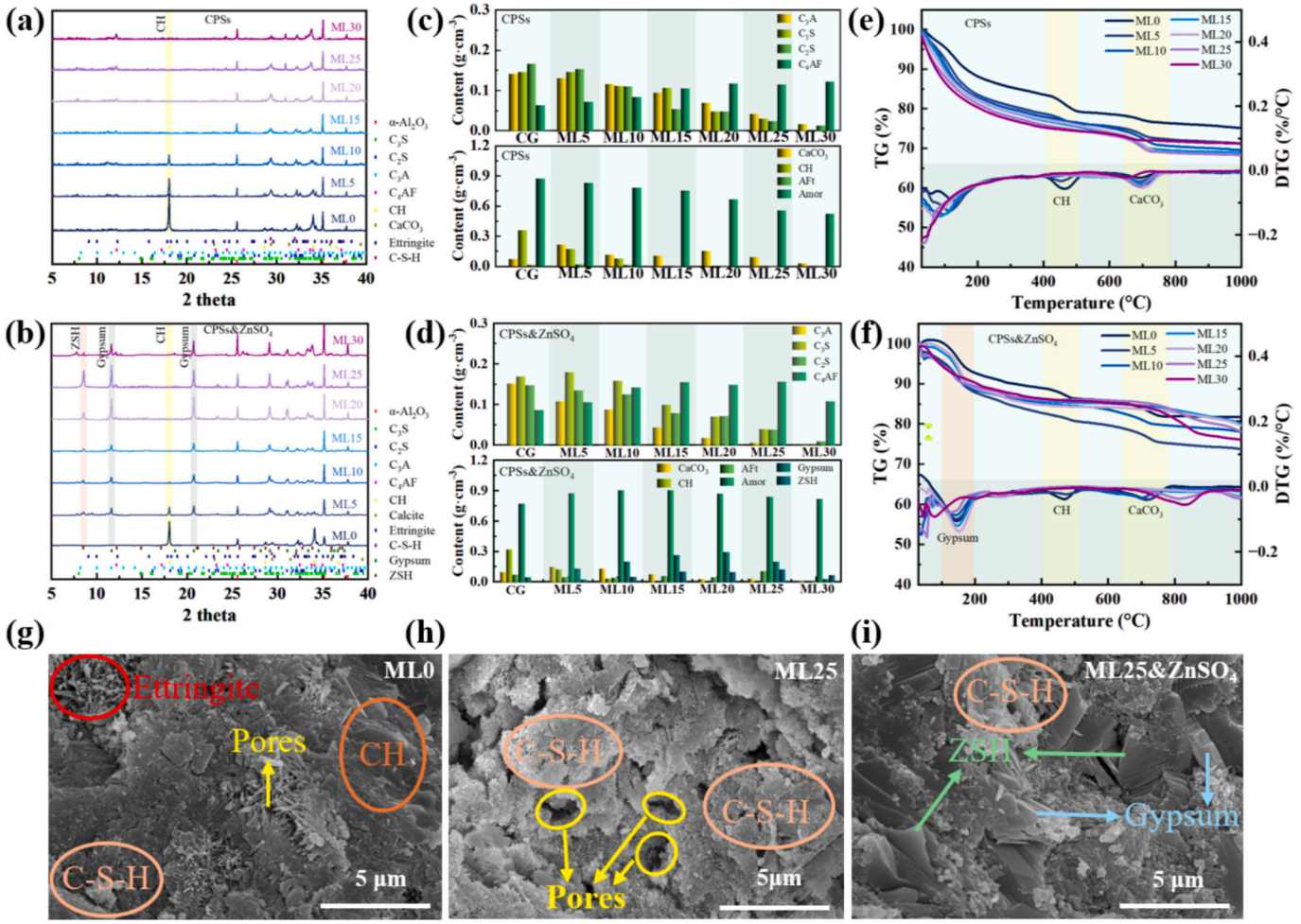


**Fig. 2.** Phase evolution and microstructural transformation of CPSs. (a, b) XRD diffraction patterns before and after $ZnSO_4$ immersion. (c, d) Quantitative phase evolution with increasing mass loss. (e, f) TG/DTG curves with different mass losses. (g-i) SEM images illustrating the transition from a dense matrix (ML0) to a porous structure (ML25) and partial re-densification after $ZnSO_4$ immersion.

substantial morphological changes, characterized by a significantly more porous structure. The C-S-H gel appears decalcified, and CH is no longer detectable, resulting in the formation of enlarged pores that often exceed several tens of microns. This transformation is primarily attributed to the progressive dissolution of calcium-rich phases, particularly CH and subsequently C-S-H, as corroborated by XRD and TG analyses in Fig. 2 (a) and (c).

Following immersion in $ZnSO_4$ electrolyte (Fig. 2 (i)), CPSs undergo further microstructural reorganization. The precipitation of newly formed crystalline phases—gypsum and ZSH—leads to partial pore infilling and a re-densified matrix structure, consistent with prior observations [26,27]. The emergence of these phases aligns with the phase identification results shown in Fig. 2 (b) and (d), confirming their role in the post-treatment morphological evolution of CPSs. SEM images in Fig. 2 (g-i) further reveal no evident cracking in the CPSs either before or after the immersion. This observation indicates that the stresses introduced during drying were effectively mitigated, resulting in minimal initial micro-crack defects.

### 3.2. Evolution of homogeneity and pore architecture

Fig. 3 (a1) presents the BSE images of CPSs, accompanied by the corresponding calcium distribution maps (Fig. 3 (a2)) and 2D pore maps (Fig. 3 (a3)), the latter extracted using Matlab. As shown in Fig. 3 (a2), calcium distribution evolves from heterogeneous in ML5–15 to increasingly uniform in ML20–30. In the ML5–15 samples, a pronounced gradient in calcium content is observed, with significantly lower concentration near the etched surface compared to the core. In contrast, this gradient largely disappears in ML20–30, indicating a more homogenous calcium distribution throughout the cross-section.

The evolution of Ca/Si ratios along the cross-section is quantified in Fig. 3 (b). With progressive etching, the Ca/Si ratio steadily declines from an initial value of 3.55 to approximately 0.72. This trend corresponds to the depletion of CH and substantial decalcification of C-S-H phase, aligning with the observations in Section 2.1. To further analyze spatial uniformity, the cross-section was evenly divided into three regions (left, middle, and right), with their respective Ca/Si ratios presented in Fig. 3 (c). As mass loss increases, the ratios converge across all regions, confirming the enhanced calcium homogeneity in samples ML25–30.

A similar trend is observed in the pore distribution, as shown in Fig. 3 (a3). From ML5–15 to ML20–30, pore structures become more uniformly distributed. The number of pore pixels rises markedly with etching, and the pores extend from the surface toward the interior. In ML5–15, pores are primarily concentrated at the edges due to localized CH dissolution. Conversely, ML20–30 exhibits a more uniform pore network across the entire cross-section. The corresponding etching depth, defined as the front of porosity development, is plotted in Fig. 3 (d). When mass loss is below 15%, the etching depth increases progressively. Beyond 15% mass loss, however, the $NH_4CI$ solution permeates the entire cross-section, indicating full penetration.

Post electrolyte immersion, Fig. 3 (a4) shows the BSE images of CPSs, while Fig. 3 (a5) maps the zinc distribution. Consistent with the trends in calcium and porosity, zinc distribution also transitions from a non-uniform pattern in ML5–15 to a more homogeneous distribution in ML20–30. In lower mass loss samples, zinc is primarily localized near the edges due to limited pore connectivity. In contrast, the ML20–30 samples display a uniform zinc distribution throughout the cross-section, facilitated by continuous pore networks. Interestingly, as shown in Fig. 3 (d), the Zn penetration depth—defined as the front of zinc concentration—lags behind the etching depth, reaching approximately 1000 um at 20% mass loss.

The cumulative porosity evolution of CPSs with varying mass loss is illustrated in Fig. 4 (a), from which total porosity ($\phi$) values were derived (Table 1). The data confirm that etching significantly increases porosity from 22.2% (ML0) to 62.0% (ML30) through selectively dissolving hydration products, particularly CH and C-S-H [32]. This increase in porosity is accompanied by a substantial rise in specific surface area, reaching 179.6 $m^2\ g^{-1}$ in ML30—an increase of 4.22 times relative to ML0. In contrast, immersion in $ZnSO_4$ electrolyte markedly reduces the porosity of etched CSPs by 30.1%, 41.3%, 33.2%, and 19.2% for ML0-ML30 samples (Table 1), due to the in situ formation of gypsum and

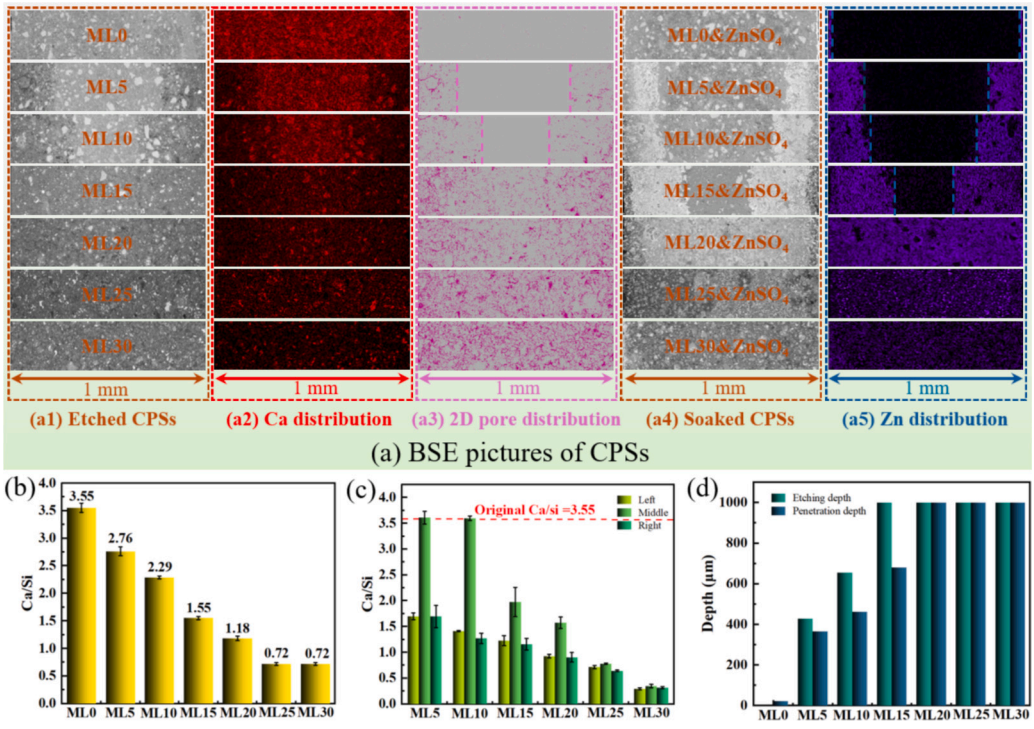


**Fig. 3.** Homogeneity analysis of CPSs: (a) BSE images; (b) Ca/Si across the full cross-section; (c) Ca/Si ratio in different regions; (d) Etching depth and zinc penetration depth.

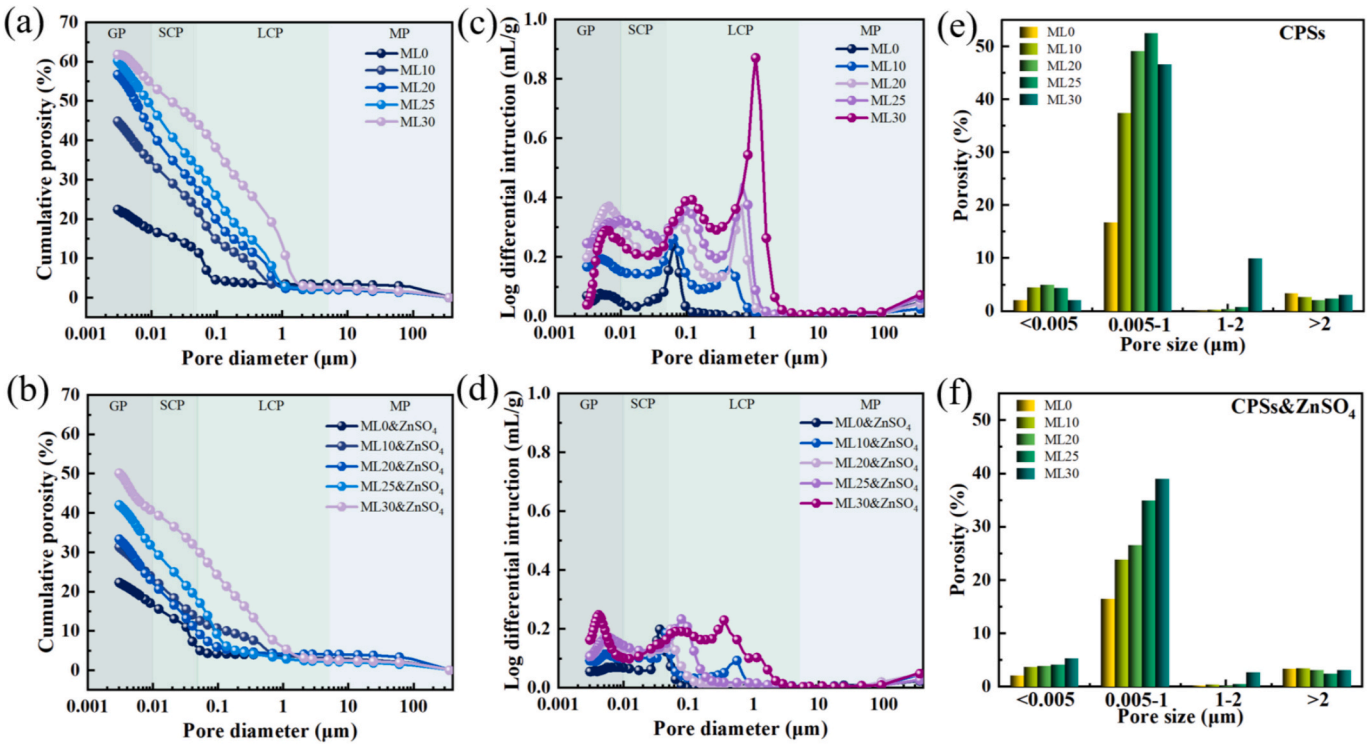


**Fig. 4.** Pore structure characteristics of CPSs before and after $ZnSO_4$ soaking: (a, b) Cumulative porosity; (c, d) Pore size distribution; (e, f) Porosity in four size ranges (<0.005 μm, 0.005–1 μm, 1–2 μm, >2 μm) before and after ZnSO4 soaking.

**Table 1**
Quantitative pore structure parameters of CPSs before and after $ZnSO_4$ electrolyte immersion.

| Parameters | ML0 | ML10 | ML20 | ML25 | ML30 |
|---|---|---|---|---|---|
| $\phi$ | 22.4 | 44.9 | 56.7 | 60.2 | 62.0 |
| $\phi^*$ | 22.3 | 31.4 | 33.3 | 40.2 | 50.1 |
| $S$ ($m^2\ g^{-1}$) | 34.4 | 96.6 | 160.3 | 163.1 | 179.6 |
| $S^*$ ($m^2\ g^{-1}$) | 36.2 | 55.4 | 72.9 | 80.9 | 93.7 |
| $d_c$ (nm) | 62.6 | 62.6 | 685.2 | 686.9 | 1118.5 |
| $d_c^*$ (nm) | 36.0 | 44.9 | 53.1 | 77.3 | 350.3 |
| $d_m$ (nm) | 46.62 | 51.77 | 54.49 | 66.92 | 191.07 |
| $d_m^*$ (nm) | 31.94 | 31.77 | 32.1 | 34.46 | 88.81 |
| $d_a$ (nm) | 16.48 | 16.21 | 15.91 | 19.11 | 31.63 |
| $d_a^*$ (nm) | 14.34 | 14.98 | 15.0 | 15.2 | 18.97 |
| $\eta$ (%) | 32.80 | 54.20 | 60.84 | 62.87 | 64.04 |
| $\eta^*$ (%) | 33.48 | 46.24 | 52.59 | 59.16 | 59.10 |
| $\tau$ | 6.48 | 3.94 | 3.33 | 3.15 | 3.05 |
| $\tau^*$ | 6.55 | 4.75 | 4.09 | 3.48 | 3.49 |

Note: * indicates values measured after immersion of CPSs in $ZnSO_4$ electrolyte.

ZSH, which fill internal pore spaces, as corroborated in Fig. 2.

Fig. 4 (c) illustrates how etching transforms the pore size distribution from a narrow single peak distribution to a broader, multi-peak patterns, indicating a more heterogeneous pore network. This multi-peak distribution persists after electrolyte immersion, albeit with a significantly lower total porosity as shown in Fig. 4 (d). The pores of CPSs are categorized into four distinct size ranges: <0.005 μm, 0.005–1 μm, 1–2 μm, and > 2 μm, and their porosity are presented in Fig. 4 (e)-(f). As mass loss increases (ML5–20), CH dissolution drives a rise in porosity within the 0.005–1 μm range, while C-S-H degradation gradually shifts pore volume from <0.005 μm to larger sizes. Beyond ML20, continuous hydration of residual cement cores generates CH (see Fig. 2 (c)), sustaining this trend. In contrast, electrolyte soaking induces densification via the formation of gypsum and ZSH phases, which partially refill etched pores (see Fig. 2 (i)). This leads to reduced pore diameter—especially in the 0.005–1 μm range (Fig. 4 (f)), although the positive correlation between mass loss and porosity (0.005–1 μm) remains evident due to prolonged immersion effects.

Three characteristic pore size parameters were also evaluated: critical diameter ($d_c$), median diameter ($d_m$), and average diameter ($d_a$). As summarized in Table 1, all parameters increase progressively with etching, reaching maxima of 1118.5 nm, 191.07 nm, and 31.63 nm, respectively, representing increases of 16.9 times, 310%, and 91.9% compared to ML0. These values decline after $ZnSO_4$ immersion, exemplified by ML25, which exhibits reductions of 88%, 13.5%, and 20.5% in the three metrics, respectively.

Additionally, Table 1 summarizes the morphological evolution of CPSs in terms of connectivity and tortuosity. Connectivity increases significantly with etching, from 32.80% (ML0) to 64.04% (ML30), representing a 95.2% improvement. Etching enhances pore connectivity by dissolving CH phases (as documented in Fig. 2), which act as fillers in capillary pores. Their removal eliminates obstructions, creating continuous percolation pathways. Conversely, tortuosity decreases from 6.48 (ML0) to 3.05 (ML30), which is achieved by removing obstructive material and aligning pores in a more linear fashion. Upon $ZnSO_4$ immersion, both parameters are adversely affected, with reduced connectivity and increased tortuosity observed across all samples, indicating densification and reduced pore accessibility (as provided in Table 1).

### 3.3. *Electrolyte uptake, ionic conductivity, and compressive strength of CPSs*

Fig. 5 (a) illustrates the electrolyte uptake of CPSs before and after $ZnSO_4$ immersion. Electrolyte uptake increases linearly with mass loss, indicating that greater degrees of etching substantially enhance $ZnSO_4$ absorption capacity. This enhancement is directly attributed to the coarsened pore structures (Table 1) that facilitate improved electrolyte retention within the CPSs matrix. Ionic conductivity of the $ZnSO_4$-soaked CPSs also shows a positive correlation with mass loss and exhibits three-stage trend. From ML0 to ML15, conductivity increases

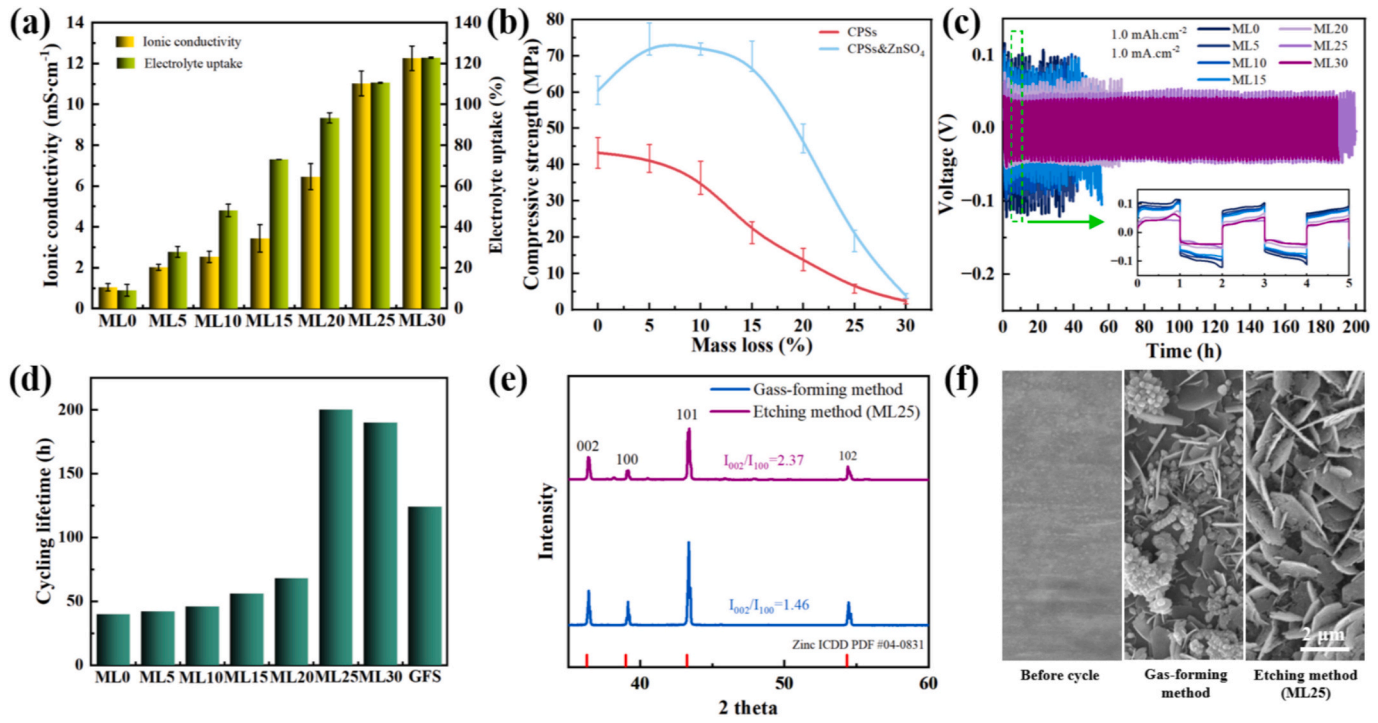


**Fig. 5.** Electrolyte uptake, ionic conductivity, mechanical strength, and Zn||Zn symmetrical cell performance of CPSs. (a) Ionic conductivity and electrolyte uptake of CPSs. (4b) Compressive strength of CPSs before and after $ZnSO_4$ immersion. (c) Cycling voltage profiles of Zn||Zn symmetrical cells with different CPSs at 1 mA $cm^{-2}$. (d) Cycling lifetimes of symmetrical cells. (e, f) XRD pattern and SEM image of zinc anode surfaces before and after cycling.

modestly by 0.83-fold. Between ML15 and ML25, it rises sharply by 2.21-fold, followed by a minor increase of 0.11-fold from ML25 to ML30. The inflection is likely due to improved etching uniformity achieved in the ML15–30 range, as evidenced by the homogeneous calcium distribution in Fig. 3 (a).

Fig. 5 (b) presents the compressive strength of CPSs before and after $ZnSO_4$ immersion. Prior to immersion, compressive strength declines sharply from 43.28 MPa (ML0) to 2.33 MPa (ML30). This reduction is attributed to the increased porosity (Table 1) and progressive decalcification of C-S-H (Fig. 2 (g-i), Fig. 3 (b-c)), which collectively reduce the load-bearing cross-sectional area and introduce more crack-prone paths. Since C-S-H is the primary strength-contributing phase in cementitious systems [41], its degradation significantly compromises mechanical integrity.

Interesting, after $ZnSO_4$ immersion, the compressive strength of CPSs improves markedly, especially for the ML5-ML25 specimens, which show over 80% increase compared to their pre-immersion counterparts. This recovery is attributed to two synergistic effects [26]: (1) in situ formation of gypsum and ZSH phases as evidenced by XRD analysis (Fig. 2); and (2) the consequent microstructural densification observed in SEM and MIP analyses (Fig. 2 and Fig. 3).

### 3.4. Electrochemical performance of Zn||Zn symmetrical cells

To evaluate the effects of CPSs on Zn plating/stripping behaviors, Zn||Zn symmetrical cells incorporating different CPSs were tested at a current density of 1 mA $cm^2$ with a constant plating capacity of 1 mAh $cm^2$, as shown in Fig. 5 (c). The enlarged figure reveals that cells employing CPSs with higher mass loss demonstrate decreased polarization voltages, yet maintain enhanced voltage stability. The cycling lifetimes of these symmetrical cells are summarized in Fig. 5 (d). A clear trend of extended cycling duration is observed with higher mass loss. While ML5–20 samples show only marginal improvement compared to ML0, the ML25-based symmetric cell exhibits substantially enhanced cycling stability, achieving over 200 h of continuous operation. The improved pore structures of CPSs promotes the uniform nucleation and growth of Zn, which reduces the polarization voltage and significantly extends the cycling life, indicating an effective mitigation of the local overpotential issue. Moreover , the symmetrical cell with ML25 exhibits a more stable cycle compared to those using gas-forming CPSs [26,27], meaning that the small pores facilitate a more uniform zinc deposition. This marked enhancement is attributed to the increased ionic conductivity (Fig. 5 (a)), uniform etching (Fig. 3 (a)) and strategically enlarged pore structure (Table 1), which together promote more homogeneous zinc deposition and stripping. Moreover, SEM analysis (see Fig. 2 (g-i) and Fig. S5) reveals that the long-term Zn||Zn symmetric cycling does not induce observable microcrack evolution within the CPS separator, and this structural stability helps to maintain the mechanical integrity of the separator, thereby supporting consistent electrochemical performance and reducing the risk of internal short circuits caused by mechanical degradation.

To further examine the influence of pore size on Zn deposition behavior, XRD analysis was performed on Zn electrodes after 20 cycles (1 mA $cm^{-2}$ at 1 mAh $cm^{-2}$) in Zn||Zn symmetric cells employing different CPSs fabricated via the gas-forming method [26] and etching method (ML25), as shown in Fig. 5 (e). The diffraction patterns are predominantly characterized by intense peaks corresponding to metallic Zn (ICDD PDF #04–0831), confirming it as the principal phase. The intensity ratio of the Zn (002) plane relative to Zn (100) planes, denoted as $I_{002}/I_{100}$, were evaluated to assess preferred orientation. The Zn (002) plane is oriented parallel to the substrate surface, whereas the Zn (100) plane exhibits a vertical alignment [42]. The $I_{002}/I_{100}$ ratio for Zn electrodes using ML25 reaches 2.37, significantly higher than the 1.46 measured for the gas-formed CPSs, indicating a more horizontally aligned growth mode of electrodeposited Zn (see Fig. 5 (f)).

### 3.5. Electrochemical performances of ZIHCs

Fig. 6 (a) illustrates the CV curves of ZIHCs assembled with CPSs of different mass loss, recorded at a sweep rate of 10 mV $s^{-1}$. The devices

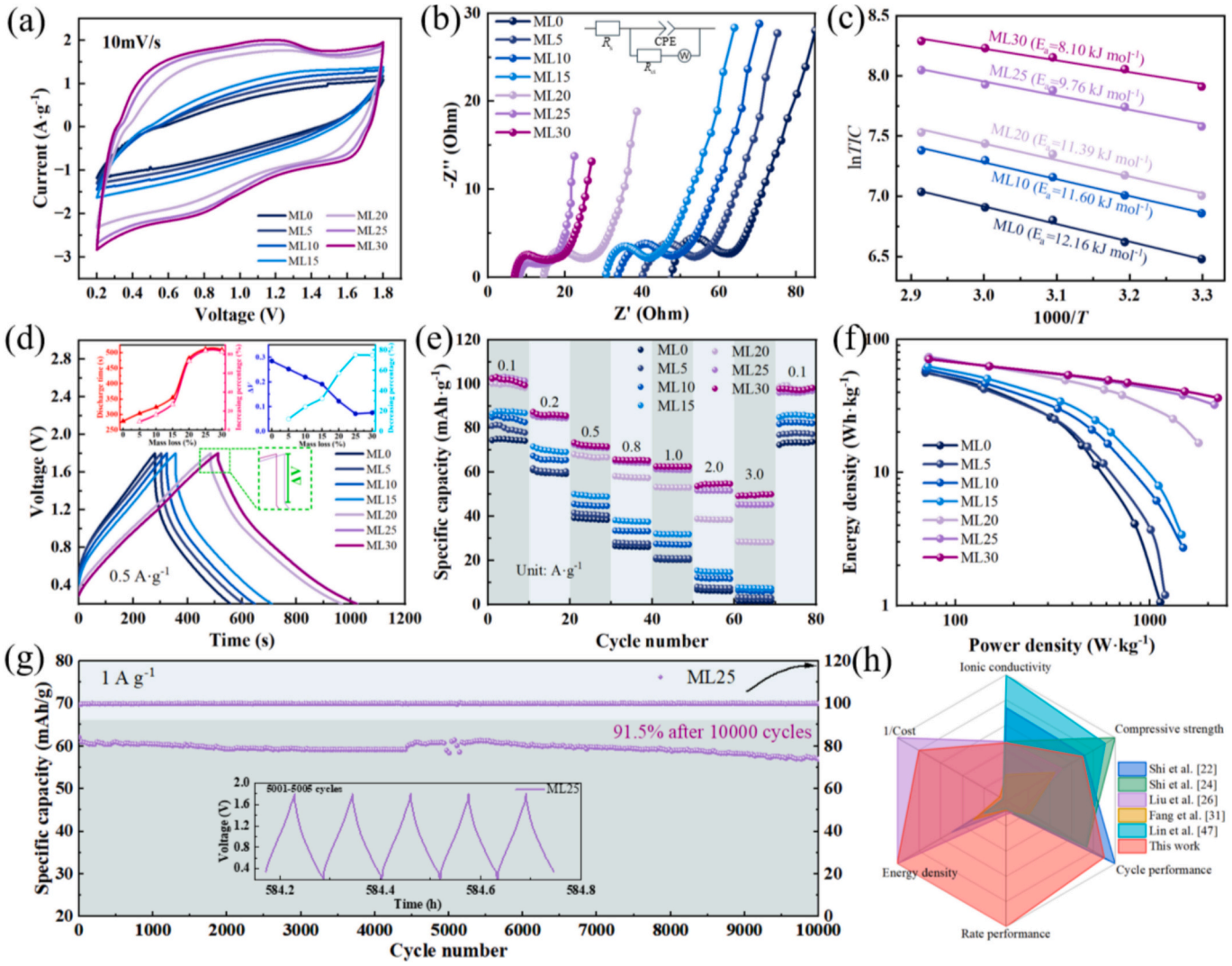


**Fig. 6.** Electrochemical performance of ZIHCs assembled with CPSs of different mass losses. (a) CV curves at 10 mV $s^{-1}$. (b) Nyquist plots with fitted equivalent circuit. (c) Arrhenius plot of bulk conductivity and corresponding activation energies ($E_a$) (d) Galvanostatic charge/discharge profiles at 0.5 A $g^{-1}$. (e) Rate performance at various current densities (0.1–3.0 A $g^{-1}$). (f) Energy density vs. power density. (g) Long-term cycling stability and coulombic efficiency of ZIHCs at 0.1 A $g^{-1}$. (h) Radar chart comparing electrochemical and mechanical performances metrics with selected representative references [22,24,26,31,47].

operate stably across a broad voltage window (0.2–1.8 V) with minimal polarization. As the mass loss increases, the CV profiles evolve from fusiform shapes without distinct redox peaks (ML0-ML15) to quasi-rectangular shapes with emerging redox features (ML20–30). This transition indicates a dual energy storage mechanism: electric double-layer capacitance from activated carbon cathodes and faradaic reactions from the zinc anodes [43–45]. The integrated CV area increases notably with progressing mass loss, showing enhanced capacity—initially moderate (ML0–15), then significantly amplified (ML20–30)—due to improved ionic conductivity (Fig. 5 (a)) from more uniform etching (Fig. 3 a) and optimized pore structures (Table 1).

Fig. 6 (b) shows the Nyquist plots of the ZIHCs, along with the fitted equivalent circuit. The high-frequency semicircle corresponds to charge-transfer resistance ($R_{ct}$) at the electrode-electrolyte interface [45], with its real-axis intercept indicating the solution resistance ($R_s$) [46], while the low-frequency linear tail reflects Warburg resistance ($R_w$), associated with ion diffusion [45]. $R_s$ decreases consistently with mass loss, confirming improved ionic conductivity (Fig. 5 (a)). Devices incorporating ML25–30 exhibit notably lower $R_{ct}$ and $R_w$, suggesting enhanced charge transfer and faster $Zn^{2+}$ diffusion due to their refined microstructure (Fig. 3 (a)) and pore connectivity (Table 1).

Fig. 6 (c) presents the Arrhenius plot of bulk conductivity for CPSs along with the corresponding activation energy ($E_a$). Here, $E_a$ refers to the energy barrier that $Zn^{2+}$ ions must overcome to migrate through the porous CPSs, involving interactions with both pore walls and the electrolyte. As shown in Fig. 8(c), electrochemical measurements indicate that the $E_a$ for $Zn^{2+}$ transport dropped markedly from 12.16 kJ $mol^{-1}$ (ML0) to 8.10 kJ $mol^{-1}$ (ML30) after the pore structure optimization of the CPSs—a reduction of approximately 33%. This reduction in $E_a$ reflects a significant enhancement in the kinetics of ion migration. A lower $E_a$ generally correlates with smoother ion transport and diminished internal resistance (as supported by Fig. 5 (a) and Fig. 6 (b)), enabling the battery to sustain higher current densities without significant polarization (see Fig. 5 (c)). These results suggest that $Zn^{2+}$ ions encounter less resistance during transport, thereby facilitating more efficient ion diffusion within the CPSs. The decline of $E_a$ can likely be ascribed to the optimized pore architecture of the CPSs (refer to Table 1), which promotes more continuous pathways for ion conduction.

Fig. 6 (d) presents the GCD profiles of ZIHCs measured at a current density of 0.5 A $g^{-1}$. The GCD curves at 0.5 A $g^{-1}$ display nearly symmetrical triangular shapes, indicative of high reversibility and capacitive behavior [48]. Discharge duration increases by 27.2% from ML0 to ML15 and by 82.9% from ML20 to ML30, aligning with the ionic conductivity trends in Fig. 5 (a). Initial voltage drop ($\Delta V$) decreases linearly

with increasing mass loss, indicating reduced resistance. The ML25-based device achieves the lowest $\Delta V$ value of 0.109 V, a 75.1% reduction relative to ML0, attributed to improved ion conductivity (Fig. 5 (a)) and relatively lower $R_s$ (Fig. 6 (b)).

Fig. 6 (e) highlights the rate performance across current densities ranging from 0.1 to 3.0 A $g^{-1}$. Specific capacity improves with increasing mass loss, especially at a higher current density. Compared to ML0, the capacity enhancement factor rises from 0.24× at 0.1 A $g^{-1}$ to 29.4× at 3.0 A $g^{-1}$. The observed improvement in rate performance can be attributed to the reduced $E_a$, which facilitates faster Zn-ion migration within the CPSs, as conformed in Fig. 6 (c).

Fig. 6 (f) illustrates the energy density of ZIHCs as a function of power density. Energy density declines with increasing power density, consistent with typical energy storage behavior. However, devices with higher mass loss maintain superior energy density. The ML25-based ZIHC achieves an impressive energy density of 73.02 Wh $kg^{-1}$ at a power density of 72.97 W $kg^{-1}$ (equivalent to 1.81 Wh $m^{-2}$ at 1.8 W $m^{-2}$). Fig. S7 compares the Ragone performance of the ML25-based ZIHCs with previously reported systems [45,49–53]. The ML25-based device outperforms most reported ZIHCs, offering higher energy density at comparable power densities. This superior performance is attributed to the use of active carbon material and optimized structural features, though it slightly trails devices utilizing modified Zn foil electrodes [50].

Overall, ML25 represents the optimal CPSs configuration, combining high ionic conductivity (12.25 mS $cm^{-1}$) and adequate compressive strength (18.93 MPa after $ZnSO_4$ immersion). The corresponding cyclic stability of ZIHCs are presented in Fig. 6 (g), delivering a high specific capacity of 102.5 mAh $g^{-1}$ at 0.1 A $g^{-1}$ (253.8 mAh $cm^{-2}$ at 0.25 mA $cm^{-2}$) and retains 91.5% capacity over 10,000 cycles, with nearly 99% coulombic efficiency. To directly verify the long-term stability of the zinc anode, SEM characterization was performed on the zinc electrodes extracted from the cycled ZIHCs (including ML15, and ML25). As shown in Fig. S6, the ML25 zinc anode exhibits a remarkably smooth, dense, and uniform surface morphology, whereas the ML15 surface remains relatively rough and uneven. The improvement can be attributed to the optimized pore structure of the CPSs achieved by the etching process, which promotes homogeneous ion flux and guides uniform nucleation. Finally, Fig. 6 (h) benchmarks this system against state-of-the-art SESSs [22,24,26,31,47], demonstrating its competitive advantages in cost, energy density, rate capability, ionic conductivity, and structural robustness.

## 4. Discussion

### 4.1. Predictive model of ionic conductivity based on pore structure

Archie's law, first introduced in 1942, stands as one of the most widely used empirical models linking the porosity and conductivity in porous media [54]. It is expressed as:

$$IC = IC_0 \phi^m \tag{13}$$

where $IC$ is the ionic conductivity, $\phi$ is the porosity, $IC_0$ is the conductivity of the pore solution, and m is a shape exponent reflecting the connectivity of the conductive phase. While useful for natural systems, Archie's law often fails to capture the complexities of engineered porous materials, such as CPSs, necessitating refinement.

To examine the role of pore characteristics in ionic conductivity, Fig. 7 (a) plots the relative conductivity ($IC/IC_0$) against the total porosity ($\phi^*$) of CPSs after immersing in electrolyte. The weak correlation ($R^2 < 0.9$) suggest that total porosity alone cannot reliably predict ionic transport, likely due to the presence of non-conductive pore that do not contribute to percolation pathways.

Considering that ionic conductivity in separators typically requires submicron pores [55,56], we performed a systematic analysis across various pore diameter ranges: 0.005–1 μm, 0.05–1 μm, 0.1–1 μm, 0.05–0.85 μm, and 0.05–0.55 μm. Fig. 7 (b-f) present the relationships between $IC/IC_0$ and porosities across these distinct pore diameter ranges. Among them, three ranges—0.005-1 μm, 0.05–1 μm, and 0.05–0.85 μm—exhibit strong linear correlation with $IC/IC_0$ ($R^2$ = 0.95–0.98), with the 0.05–0.85 μm range showing the strongest

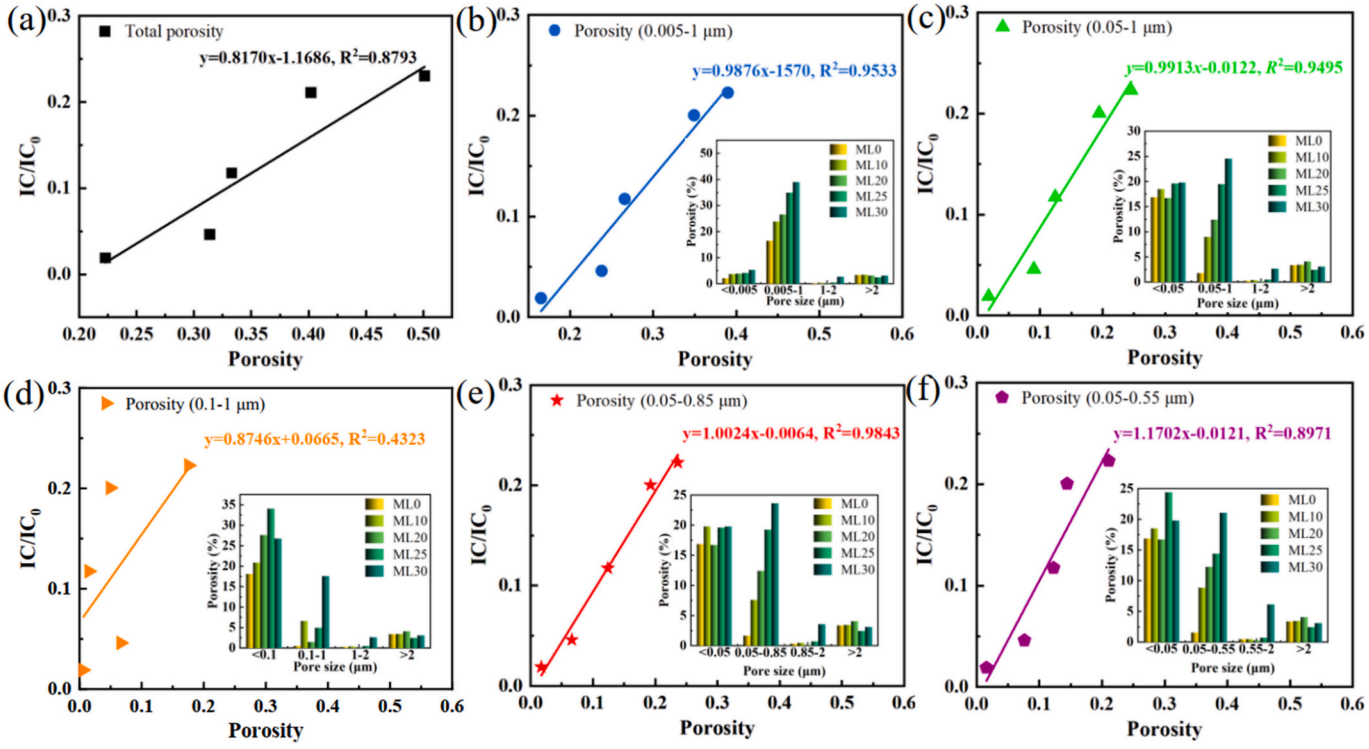


**Fig. 7.** The relationship between the porosity and ionic conductivity of CPSs.

correlation ($R^2$ = 0.98, Fig. 7 (e)). In contrast, narrower or broader ranges such as 0.1–1 μm and 0.05–0.55 μm yield lower correlation coefficients ($R^2$ = 0.43 and 0.89, respectively), indicating that pores outside this optimal window may either disrupt connectivity or impeded ion mobility due to strong ion-wall interactions. Accordingly, we propose a modified Archie-type model:

$$IC = IC_0 \phi_{0.05-0.85\mu m} \quad (14)$$

where $\phi_{0.05-0.85\mu m}$ represents the porosity contributed by pores within 0.05–0.85 μm, and m = 1, as derived from the slope in Fig. 7 (e). This formulation reflects an effective medium approximation, in which only the optimally sized pores contribute to ionic transport.

To illustrate the applicability of the model, Fig. 8 (a) presents the relationship between pore connectivity and porosity from this work and other pore regulation techniques [22,25–27,30,31]. A connectivity factor $\lambda = \phi_{<1\mu m}/\phi^*$ was introduced to compare the pore connectivity of etched CPSs with those modified by other reported techniques. Two distinct regions emerge: $\lambda < 0.80$ and $\lambda > 0.80$. Etched CPSs exhibit significantly higher $\lambda$ at similar porosity, indicating superior ion transport efficiency. Specifically, when the mass loss is 25% or greater, $\lambda$ value exceeds 90%. Fig. 8 (b) compares predicted and measured conductivities from this work and literature [26]. For systems with $\lambda > 0.80$, our model yields excellent agreement, achieving a root mean square error (RMSE) of 0.65. However, it performs less accurately for literature data [26] with $\lambda < 0.80$ (RMSE = 9.86), likely due to differences in pore morphology or incomplete electrolyte infiltration.

When the sample is completely immersed in the electrolyte, the model is therefore valid for porous materials where >80% of pores fall below 0.85 um in diameter. The identified effective range (0.05–0.85 μm) is consistent with findings in other porous systems where efficient ion transport is governed by submicron connective pathways [55,56], underscoring the importance of this scale for constructing percolating conductive networks. However, its reliance hinges on the assumption of complete electrolyte wetting, which may not apply to hydrophobic or poorly infiltrated porous networks.

### 4.2. *Effects of pore structures on electric field profile and zinc concentration distribution*

Based on the finite element simulations, this study elucidates the critical role of pore size, porosity, and pore connectivity within CPSs in governing the spatial distribution of the electric field (Fig. 9 (a-c)) and $Zn^{2+}$ concentration (Fig. 9 (d-f)). As depicted in Fig. 9 (a, d), the M1 model, featuring large pore size, displays a strongly inhomogeneous electric field with localized regions of elevated current density (hot zones in red/yellow) and pronounced $Zn^{2+}$ concentration gradients. Such spatially concentrated electric fields inevitably generate locally elevated interfacial overpotentials, which promote preferential $Zn^{2+}$ reduction at protruding sites and amplify tip-enhanced growth. In contrast, the M2 model in Fig. 9 (b, e), with small pore size, exhibits a more moderated electric field distribution and attenuated ion

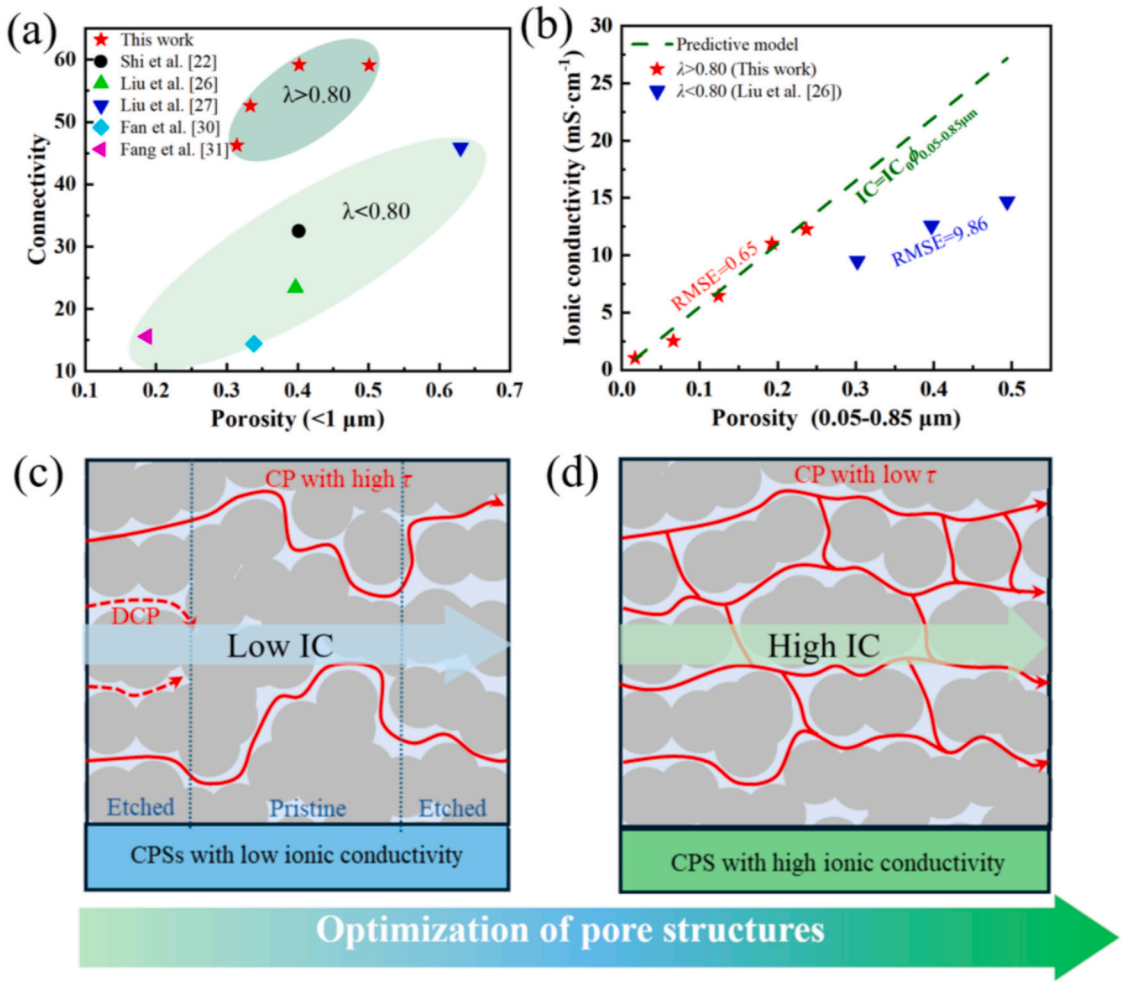


**Fig. 8.** (a) Relationship between pore connectivity and porosity of CPSs with literature data [22,26,27,30,31]. (b) Comparation between predicted and measured ionic conductivities [26]. (c-d) Schematic illustration of pore structure optimization in CPSs. (Note: DCP: discontinuous conduction pathways; CP: continuous conduction pathways);

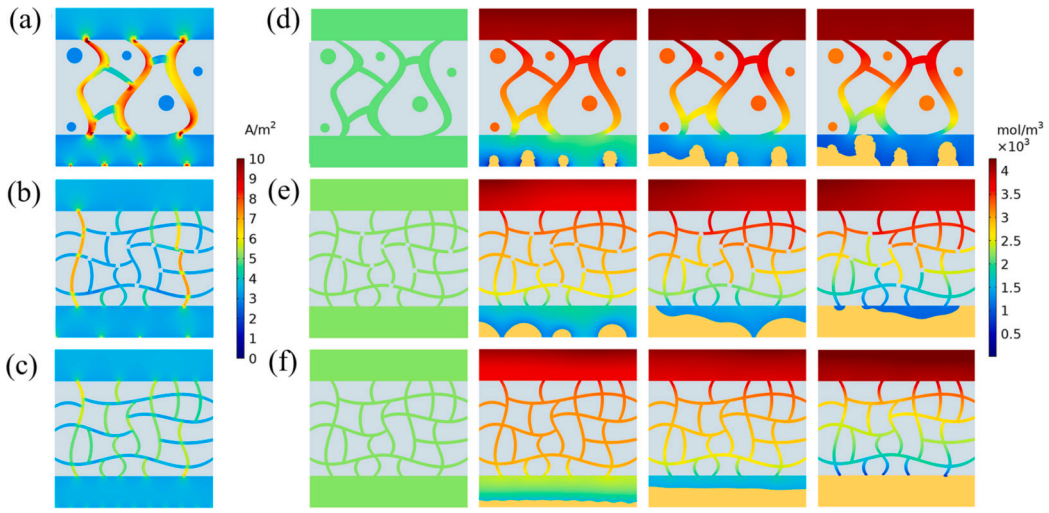


**Fig. 9.** Modeling and simulation analysis of pore connectivity and ion transport behavior in CPSs. (a-c) Simulated electric field distributions of three separator models with varying pore size, porosity and connectivity: Model M1 (large pore size, high porosity, and low connectivity), Model M2 (micropore, threshold porosity, and lower connectivity relative to ML20), and Model M3 (micropore, high porosity, and high connectivity relative to ML25). (e-f) Simulated $Zn^{2+}$ concentration profiles corresponding to these models in (e-g).

concentration polarization, reflecting a certain degree of improvement in ion transport uniformity. Most notably, the M3 model—designed with small pore size, high porosity, and high connectivity—presents the most uniform electric field distribution and near-uniform $Zn^{2+}$ concentration distribution throughout the simulation period, as shown in Fig. 9 (c, f). This optimized configuration effectively mitigates localized $Zn^{2+}$ accumulation and eliminates steep electric field gradients, minimizing local overpotential fluctuations and equalizing the probability of Zn nucleation across the electrode surface. As a result, Zn growth proceeds in a more regulated manner, suppressing crystallographic anisotropy and dendrite-prone growth modes.

The simulated results are strongly corroborated by experimental evidence. The Zn||Zn symmetric cells using CPSs with large pore size and non-uniform pore size distribution demonstrate highly fluctuating polarization voltages [26,27], which aligns well with the simulation results from the M1 model. In comparison, cells incorporating highly porous, microporous CPSs (ML0-ML25) exhibit constantly strengthening cycling stability with progressively decreasing voltage fluctuation (Fig. 5 (c)) and decreasing activation energy (Fig. 6 (c)), verifying the suppression of local current concentration predicted by the M2 and M3 model. The simulation results also indicate that three-dimensional interconnected multiscale pores (M3) facilitate ion transport and uniform zinc deposition, which is highly consistent with the results of the predictive model in section 4.1 and analysis of zinc (002) plane (see Fig. 5 (e)). Together, these results collectively confirm that pore size, porosity and connectivity govern not only the spatial uniformity of both the electric field and $Zn^{2+}$ distribution, but also the interfacial nucleation environment that dictates Zn growth behavior, underpinning the proposed continuous channel conduction mechanism that bridges microstructural regulation and interfacial stability in zinc metal systems. This mechanism highlights the critical role of pore structure engineering—complementary to the dielectric property modulation of separators [57]—in achieving homogeneous ion transport and deposition.

### 4.3. *Effects of pore structures on electrochemical performances of ZIHCs*

Fig. 1 (b) illustrates the dual energy storage mechanism of ZIHCs, which involves electric double-layer capacitance (EDLC) from ion adsorption/desorption at the activated carbon cathode and Faradaic reactions via zinc deposition/stripping at the zinc anode [43–45]. The efficiency of this dual mechanism—and thus the overall electrochemical performance of ZIHCs—is highly dependent on the ionic conductivity of the CPSs, which is governed primarily by their pore structure characteristics and uniformity [56].

As shown in Fig. 8 (c), CPSs with low mass loss (<25%) exhibit non-uniform etching and underdeveloped pore networks. These samples feature gradient pore distribution and discontinuous diffusion pathways, which result in only marginal increases in porosity and pore connectivity, along with a limited reduction in tortuosity and activation energy (Fig. 3 (a3), Fig. 6 (c) and Table 1). Their poor electrolyte retention capacity (Fig. 5 (a)), and limited effective pore fraction within the critical 0.05–0.85 μm range (<20%, Fig. 8 (b)) collectively restrict ion mobility, leading to low ionic conductivity and thus compromised electrochemical performance. Although the ML20 sample displayed uniform pore structures prior to electrolyte immersion (Fig. 3 (a)), slight re-densification post-electrolyte immersion (see Fig. 3 and Table 1) compromises its performance, making its heterogeneous zinc deposition and stripping, conformed by the simulation in Fig. 9 (b, e).

In contrast, CPSs with higher mass loss (≥25%) demonstrate well-developed, uniform pore structures and superior electrochemical properties (Fig. 8 (d)). These samples exhibit enhanced porosity, broader pore size distribution, improved interconnectivity, lower tortuosity, and declined activation energy (Fig. 3 (a3), Fig. 6 (c) and Table 1), enabling rapid ion transport and continuous conductive pathways. Their electrolyte retention capacity improves markedly (Fig. 5 (a)), with their $\lambda$ values surpassing 90% and their porosities within the 0.05–0.85 μm range exceeding 20% (see Fig. 8 (a, b)). These features collectively contribute to enhanced ionic conductivity of CPSs (Fig. 5 (a)), promote more homogeneous zinc deposition and stripping (see Fig. 5 (c) and Fig. 9 (c,f)) which translates to superior ZIHC performances, as systematically demonstrated in Fig. 6. The progressive electrochemical enhancement—from moderate to pronounced—confirms the pivotal role of controlled pore structural tuning via etching process. This study highlights pore structure optimization as a viable strategy for developing high-performance SESSs.

In practical operation, the pore structures of CPSs critically determine the environmental stability and lifespan of ZIHCs. Specifically, the pore-engineered CPSs features open channels that enhance ionic conductivity (see Fig. 5 (a)) while also serving as primary pathways for environmental exchange. Under dry or low-humidity conditions, the high specific surface area of CPSs can accelerate electrolyte evaporation, which may lead to a “dry-out failure” mode characterized by increased internal resistance. In contrast, in humid or aqueous environments, the

same porous network could allow the ingress of moisture and impurity ions (e.g., $Na^+$, $Cl^-$), resulting in electrolyte dilution, contamination, and interfacial electrochemical disturbance, potentially triggering a "contamination failure" mode marked by rapid capacity fade, high self-discharge, and voltage instability. Therefore, the ability of the separator to balance efficient $Zn^{2+}$ transport with effective environmental sealing is essential for the environmental adaptability and long-term cycling performance of ZIHCs.

## 5. Conclusions

This study presents a controlled fabrication strategy for porous CPSs via a selective etching method that enables the precise dissolution of hydration products. Systematic characterization reveals that the etching method effectively modulates pore structure by preferentially increasing porosity within the 0.005–1.0 μm range. Subsequent electrolyte immersion partially reduces these enhanced pores, yet maintains superior porosity compared to pristine cement paste. A porosity-conductivity correlation predictive model was established based on Archie's law, identifying the 0.05–0.85 μm pore range as the critical factor of ionic transport. The optimized CPSs with 25% mass loss exhibit remarkable structural improvements, including notably enhanced porosity, more uniform pore distribution, increased connectivity, and reduced tortuosity, along with the decrease in activation energy. Notably, over 90% of the pores are smaller than 0.85 μm in diameter. These structural enhancements collectively contribute to a high ion conduction of 12.25 mS $cm^{-1}$ alongside an acceptable mechanical robustness of 18.93 MPa. The optimized CPSs promote highly stable zinc deposition and stripping, as evidenced by minimal voltage fluctuation in Zn||Zn symmetrical cells and direct confirmation via finite element simulations. The constructed ZIHCs achieves excellent metrics with a splendid rate performance, an excellent specific capacity of 103.2 mAh $g^{-1}$ at 0.1 A $g^{-1}$, an outstanding energy density of 73.02 Wh $kg^{-1}$ at power density of 72.97 W $kg^{-1}$ and ultralong cycling stability with a capacitance retention of 91.5% over 10,000 cycles at a current density of 1 A $g^{-1}$.

Looking forward, the fundamental strategy of employing etching-based controllable porous CPSs is not limited to ZIHCs. A highly promising goal is to extend its application to high-capacity AZIBs employing manganese-based or vanadium-based cathodes. The etched porous structure may act as a physical sieve, confining the dissolution of $Mn^{2+}$ or V-species to suppress cathode degradation. Its mechanical robustness and electrolyte wettability enable stable long-term operation in aqueous electrolytes. This extension underscores the universal value of our separator design for next-generation aqueous energy storage systems, pointing toward its potential applicability beyond ZIHCs. Such progress could facilitate the integration of our devices as functional components for energy storage within future smart and multifunctional infrastructure. In addition, while this study demonstrates the promising electrochemical performance of chemically-etched CPSs in ZIHCs, we acknowledge that its practical implementation in real-world structural energy storage systems faces significant challenges.

## CRediT authorship contribution statement

**Guanghui Tao:** Writing – original draft, Investigation, Formal analysis, Data curation. **Yurong You:** Validation, Project administration, Formal analysis. **Zhaolong Liu:** Methodology, Investigation. **Shuyang Bian:** Visualization, Formal analysis. **Ruidan Liu:** Methodology, Investigation. **Long Yuan:** Investigation, Conceptualization. **Jian Chen:** Validation, Software. **Linfeng Hu:** Supervision, Conceptualization. **Pan Feng:** Writing – review & editing, Supervision, Resources.

## Declaration of competing interest

The authors declare that they have no known competing financial interests or personal relationships that could have appeared to influence the work reported in this paper.

## Acknowledgements

This work was supported by the National Key Research and Development Program of China (No. 2024YFB3715000), National Natural Science Foundation of China (No. 52478238), Science and Technology Program Special Fund of Jiangsu Province (Frontier Leading Technology Basic Research) Major projects (No. BK20222004).

## Appendix A. Supplementary data

Supplementary data to this article can be found online at https://doi.org/10.1016/j.est.2026.121058.

## Data availability

Data will be made available on request.

## References

[1] Q. Zhao, T. Xu, K. Liu, H. Du, M. Zhang, Y. Wang, L. Yang, H. Zhang, X. Wang, C. Si, Biomass-based functional materials for rechargeable Zn-ion batteries, Energy Storage Mater. 71 (2024) 103605.
[2] A. Emin, A. Ding, M. Mateen, S. Tul Muntaha, A. Parkash, S. Ali, Q. Li, An efficient electrodeposition approach for preparing CoMn-hydroxide on nickel foam as high-performance electrodes in aqueous hybrid supercapacitors, Fuel 381 (2025) 133335.
[3] H. Jiang, M. Jin, L. Sun, D. Huang, P. Guo, J. Li, H. Zhu, Y. Wang, Boosting the performance of Zn ion hybrid supercapacitors by regulating the chemically and physically active sites of graphene films, Dalton Trans. 53 (36) (2024) 15236–15245.
[4] L. Zhao, S. Zhao, N. Zhang, P. Wang, Z. Liu, Y. Xie, J. Shu, T. Yi, Construction of stable Zn metal anode by inorganic functional protective layer toward long-life aqueous Zn-ion battery, Energy Storage Mater. 71 (2024) 103628.
[5] X. Ni, Y. Zhao, P. Cai, Q. Xu, D. Li, Biomass-tar-derived oxygen-enriched porous carbon as a high-performance carbon electrode material for double electric layer and zinc-ion hybrid supercapacitor, Diam. Relat. Mater. 148 (2024) 111451.
[6] M. Hasan, S. Sahoo, D.R. Kumar, R. Karthik, G. Dhakal, J. Lee, Y. Kim, J. Shim, Defect engineering of Mn-substituted KNiF3 perovskite fluoride for high-performance asymmetric hybrid supercapacitors, J. Energy Storage 97 (2024) 112925.
[7] J. Zhu, J. Tai, T. Liu, Y. Wang, Y. Li, M. Yang, D. Ma, L. Deng, J. Luo, P. Zhang, Emerging Zinc-Ion Capacitor Science: Compatible Principle, Design Paradigm, and Frontier Applications, Advanced Energy Materials (2024) 2403739.
[8] Z. Hao, Y. Dai, X. Xu, X. Zhao, Y. Cong, X. Wu, W. Zhou, Strategies for addressing the challenges of aqueous zinc batteries enabled by functional separators, J. Mater. Chem. A 11 (21) (2023) 11031–11,047.
[9] W. Zhou, M. Yang, M. Chen, G. Zhang, X. Han, J. Chen, D. Ma, P. Zhang, Ion-Sieving Effect Enabled by Sulfonation of Cellulose Separator Realizing Dendrite-Free Zn Deposition, Adv. Funct. Mater. 34 (27) (2024) 2315444.
[10] W. Zhou, M. Chen, Q. Tian, J. Chen, X. Xu, C.-P. Wong, Cotton-derived cellulose film as a dendrite-inhibiting separator to stabilize the zinc metal anode of aqueous zinc ion batteries, Energy Storage Mater. 44 (2022) 57–65.
[11] H. Ma, H. Chen, M. Chen, A. Li, X. Han, D. Ma, P. Zhang, J. Chen, Biomimetic and biodegradable separator with high modulus and large ionic conductivity enables dendrite-free zinc-ion batteries, Nat. Commun. 16 (1) (2025) 1014.
[12] C. Gao, H. Zeng, J. Xu, D. Xu, Y. Ma, W. She, Z. Hu, J. Tang, J. Liu, Collaborative enhancement in "strength-toughness-elastic modulus" of calcium-silicate-hydrate (C-S-H) based organic-inorganic composites: Chemical bonding and cracking path optimization, Cem. Concr. Res. 187 (2025).
[13] Q. Meng, D.D.L. Chung, Battery in the form of a cement-matrix composite, Cem. Concr. Compos. 32 (10) (2010) 829–839.
[14] P. Feng, Z. Liu, L. Yuan, X. Liu, R. Liu, G. Tao, Z. Yu, X. Meng, J. Chen, Q. Ran, J. Hong, C. Miao, Y. Lu, J. Liu, Concrete: From infrastructure to structural energy storage, Mater. Today 91 (2025) 364–374.
[15] M. Shi, L. Wang, D. Zhang, Implementation of durable structural supercapacitors with molybdate-ion-intercalated NiCo-LDH and polymer-cement composite, Compos. Part B 295 (2025) 112209.
[16] S. Zhu, Y. Sun, K. Li, Y. Dang, X. Guan, Construction of structural supercapacitor with high energy density and mechanical strength based on dual-carbon electrodes and polyacrylamide-Portland cement-Na2SO4 electrolyte, J. Power Sources 597 (2024) 234150.
[17] J. Wang, P. Zhan, D. Zhang, Redox active cement-based electrolyte toward high-voltage asymmetric solid supercapacitor, Cem. Concr. Compos. 138 (2023) 104987.
[18] J. Wang, P. Zhan, D. Zhang, L. Tang, Nickel cobalt sulfide composite nanosheet anchored on rGO as effective electrode for quasi-solid supercapacitor, J. Energy Storage 70 (2023) 107938.

[19] S. Araby, B. Philips, Q. Meng, J. Ma, T. Laoui, C.H. Wang, Recent advances in carbon-based nanomaterials for flame retardant polymers and composites, Compos. Part B 212 (2021) 108675.
[20] W. Chen, T. Lei, C. Wu, M. Deng, C. Gong, K. Hu, Y. Ma, L. Dai, W. Lv, W. He, X. Liu, J. Xiong, C. Yan, Designing Safe Electrolyte Systems for a High-Stability Lithium-Sulfur Battery, Adv. Energy Mater. 8 (10) (2018) 1702348.
[21] J. Zhang, J. Xu, D. Zhang, A Structural Supercapacitor Based on Graphene and Hardened Cement Paste, J. Electrochem. Soc. 163 (3) (2015) 83–87.
[22] M. Shi, D. Zhang, Integrated construction improving electrochemical performance of loadable supercapacitors based on porous cement-based solid electrolytes, J. Power Sources 616 (2024) 235135.
[23] C. Zhou, Q. Wang, C. Zhang, Electrochemical Energy Storage Properties of High-Porosity Foamed Cement, Materials 15 (7) (2022) 2459.
[24] M. Shi, D. Zhang, 3D porous cementitious electrolytes with "stream-reservoir" ionic channels for high multifunctional performance structural supercapacitors, J. Mater. Chem. A 12 (4) (2024) 2237–2248.
[25] W. Ma, D. Zhang, Preparation of porous magnesium phosphate material and its application in structural supercapacitors, CIESC Journal 69 (10) (2018) 4438–4448.
[26] Z. Liu, P. Feng, R. Liu, L. Yuan, X. Meng, G. Tao, J. Chen, Q. Ran, J. Hong, J. Liu, C. Miao, Integration of zinc anode and cement: unlocking scalable energy storage, National Science Review 11 (10) (2024) nwae309.
[27] R. Liu, P. Feng, Z. Liu, L. Yuan, G. Tao, Z. Yu, X. Meng, J. Chen, An innovative structural energy storage solution using fly ash-cement composites for net-zero energy buildings, Cem. Concr. Compos. 157 (2025) 105960.
[28] Y. Zong, H. He, Y. Wang, M. Wu, X. Ren, Z. Bai, N. Wang, X. Ning, S.X. Dou, Functionalized Separator Strategies toward Advanced Aqueous Zinc-Ion Batteries, Adv. Energy Mater. 13 (20) (2023) 2300403.
[29] E.P. Kearsley, P.J. Wainwright, The effect of porosity on the strength of foamed concrete, Cem. Concr. Res. 32 (2) (2002) 233–239.
[30] D. Fan, C. Zhang, J. Lu, L. Peng, R. Yu, C.S. Poon, Rheology dependent pore structure optimization of high-performance foam concrete, Cem. Concr. Res. 188 (2025) 107737.
[31] C. Fang, D. Zhang, Pore forming with hemp fiber for magnesium phosphate structural supercapacitor, Mater. Des. 186 (2020) 108322.
[32] H. Di, X. Guan, S. Liu, Changes in mechanical performance and pore structure of hardened cement paste under the combined effect of calcium leaching and dry/wet cycles, Constr. Build. Mater. 407 (2023) 133519.
[33] Y. Chen, F. Al-Neshawy, J. Punkki, Investigation on the effect of entrained air on pore structure in hardened concrete using MIP, Constr. Build. Mater. 292 (2021) 123441.
[34] Y. Zhang, Z. Yang, G. Ye, Dependence of unsaturated chloride diffusion on the pore structure in cementitious materials, Cem. Concr. Res. 127 (2020) 105919.
[35] C. Salmas, G. Androutsopoulos, Mercury Porosimetry: Contact Angle Hysteresis of Materials with Controlled Pore Structure, J. Colloid Interface Sci. 239 (1) (2001) 178–189.
[36] F. Zhi, J. Yang, G. Yang, L. Zhang, W. Li, L. Jiang, Investigation on the calcium leaching behaviors of cellulose ethers containing cement pastes, Cem. Concr. Compos. 154 (2024) 105797.
[37] Y. Yang, P. Tian, T. Gao, J. Xu, Q. Xu, H. Pang, J. Ye, G. Ning, Synthesis of controlled-particle-size boehmite for coating lithium-ion battery separators, New J. Chem. 47 (5) (2023) 2211–2220.
[38] H. Yang, L. Jiang, Y. Zhang, Q. Pu, Y. Xu, Predicting the calcium leaching behavior of cement pastes in aggressive environments, Constr. Build. Mater. 29 (2012) 88–96.
[39] M. Moranville, S. Kamali, E. Guillon, Physicochemical equilibria of cement-based materials in aggressive environments—experiment and modeling, Cem. Concr. Res. 34 (9) (2004) 1569–1578.
[40] J.J. Chen, J.J. Thomas, H.M. Jennings, Decalcification shrinkage of cement paste, Cem. Concr. Res. 36 (5) (2006) 801–809.
[41] S. He, J. Chai, Y. Yang, J. Cao, Y. Qin, Z. Xu, Effect of nano-reinforcing phase on the early hydration of cement paste: A review, Constr. Build. Mater. 367 (2023) 130147.
[42] T. Zhao, P. Xiao, S. Nie, J. Yu, S. Peng, J. Chen, F. Luo, Y. Chen, Innovative bacterial cellulose and UiO-66 composites for superior zinc ion battery separator performance, Green Chem. 27 (31) (2025) 9541–9558.
[43] Z. Dang, X. Li, Y. Li, L. Dong, Heteroatom-rich carbon cathodes toward high-performance flexible zinc-ion hybrid supercapacitors, J. Colloid Interface Sci. 644 (2023) 221–229.
[44] X. Zhang, X. Tian, Y. Song, J. Wu, T. Yang, Z. Liu, High-performance activated carbon cathodes from green cokes for Zn-ion hybrid supercapacitors, Fuel 310 (2022) 122485.
[45] S. Zeng, X. Shi, D. Zheng, C. Yao, F. Wang, W. Xu, X. Lu, Molten salt assisted synthesis of pitch derived carbon for Zn ion hybrid supercapacitors, Mater. Res. Bull. 135 (2021) 111134.
[46] C. Robinson, V.B. Juska, A. O'Riordan, Surface chemistry applications and development of immunosensors using electrochemical impedance spectroscopy: A comprehensive review, Environ. Res. 237 (2023) 116877.
[47] W. Lin, J. Xing, Y. Zhou, L. Pan, L. Yang, Y. Zhang, X.X. Liu, C. Xiong, W. Li, Z. Sun, A Biomimetic Cement-Based Solid-State Electrolyte with Both High Strength and Ionic Conductivity for Self-Energy-Storage Buildings, Research 7 (2024) 0379.
[48] Z. Pan, Y. Qiu, J. Yang, F. Ye, Y. Xu, X. Zhang, M. Liu, Y. Zhang, Ultra-endurance flexible all-solid-state asymmetric supercapacitors based on three-dimensionally coated MnOx nanosheets on nanoporous current collectors, Nano Energy 26 (2016) 610–619.
[49] H. Wang, M. Wang, Y. Tang, A novel zinc-ion hybrid supercapacitor for long-life and low-cost energy storage applications, Energy Storage Mater. 13 (2018) 1–7.
[50] D. Han, S. Wu, S. Zhang, Y. Deng, C. Cui, L. Zhang, Y. Long, H. Li, Y. Tao, Z. Weng, Q.H. Yang, F. Kang, A Corrosion-Resistant and Dendrite-Free Zinc Metal Anode in Aqueous Systems, Small 16 (29) (2020) 2001736.
[51] Y. Liu, H. Tan, Z. Tan, X. Cheng, Rice husk-derived carbon materials for aqueous Zn-ion hybrid supercapacitors, Appl. Surf. Sci. 608 (2023) 155215.
[52] H. Chen, Y. Zheng, X. Zhu, W. Hong, Y. Tong, Y. Lu, G. Pei, Y. Pang, Z. Shen, C. Guan, Bamboo-derived porous carbons for Zn-ion hybrid supercapacitors, Mater. Res. Bull. 139 (2021) 111281.
[53] T. Xiong, Y. Shen, W.S.V. Lee, J. Xue, Metal Organic framework derived carbon for ultrahigh power and long cyclic life aqueous Zn ion capacitor, Nano Materials Science 2 (2) (2020) 159–163.
[54] G.E. Archie, The electrical resistivity log as an aid in determining some reservoir characteristics, Trans. AIME 146 (01) (1942) 54–62.
[55] D.R. Rajagopalan Kannan, P.K. Terala, P.L. Moss, M.H. Weatherspoon, Analysis of the Separator Thickness and Porosity on the Performance of Lithium-Ion Batteries, International Journal of Electrochemistry 2018 (2018) 1–7.
[56] C.F.J. Francis, I.L. Kyratzis, A.S. Best, Lithium-Ion Battery Separators for Ionic-Liquid Electrolytes: A Review, Adv. Mater. 32 (18) (2020) 1904205.
[57] L.N.u. Rehman, Y. Zhou, A. Saleem, T. Mehmood, G.S. dos Reis, Development of a Janus cellulose separator with dielectric effect modulation using 2D perforated titania nanosheet for zinc batteries, J. Power Sources 660 (2025) 238412.